Revision 2

Magnetite-rutile symplectite in ilmenite records magma hydration in layered intrusions

Wei Tan[1, 2, 3], Christina Yan Wang[1, 2], Steven M. Reddy[3, 4], Hongping He[1, 2]*, Haiyang Xian[1, 2], Changming Xing[1, 2]

[1]CAS Key Laboratory of Mineralogy and Metallogeny/Guangdong Provincial Key Laboratory of Mineral Physics and Materials, Guangzhou Institute of Geochemistry, Chinese Academy of Sciences, Guangzhou 510640, China

[2]CAS Center for Excellence in Deep Earth Science, Guangzhou, 510640, China

[3]School of Earth and Planetary Sciences, The Institute for Geoscience Research (TIGeR), Curtin University, GPO Box U1987, Perth, WA 6845, Australia

[4] Geoscience Atom Probe, John de Laeter Centre, Curtin University, GPO Box U1987, Perth, WA 6845, Australia

Abstract

The textures and geochemical characteristics of the rocks in layered intrusions potentially provide insights into the physico-chemical processes that have taken place in mafic magma chambers. Diverse exsolution textures of Fe-Ti oxides in layered intrusions may record the variation of sub-solidus temperature and oxygen fugacity (fO_2) of cooling magma chambers. Here we investigated ilmenite-hematite solid solution (Ilm_{ss}) relationships evident in preserved intergrowths of magnetite-rutile and ilmenite-hematite in the gabbro of the Xinjie layered intrusion. The crystallographic orientation and 3-D morphology of the two intergrowth types constrain the transformation mechanism of the exsolution textures from Ilm_{ss}. The results reveal that the interface of the ilmenite-hematite intergrowth is more energetically favorable than that of the magnetite-rutile symplectite when they are transformed from Ilm_{ss} on cooling. The QUILF equilibria suggests that the magnetite-rutile symplectite can be transformed from Ti-rich ilmenite with $Ilm_{\geq 0.85}$ above 550°C when the sub-solidus T-fO_2 trend is buffered by the biotite-ilmenite-feldspar-ulvöspinel (KUIlB) mineral assemblages crystallized from hydrated mafic magmas. The magnetite-rutile symplectite can be then taken as a unique texture indicator of magma hydration in the evolution history of terrestrial, martian and lunar magmas.

Key Words: Magnetite-rutile symplectite; ilmenite-hematite solid solution (Ilm_{ss}); magma hydration; layered intrusion

Introduction

Layered intrusions preserve the fully crystalline products of magmas that may have experienced different physicochemical processes in mafic magma chambers (*e.g.*, Holness et al. 2017 and references therein). One fundamental aspect on the petrogenesis of layered intrusions that remains controversial is the link between rock textures and magmatic processes (McBirney and Hunter 1995; Latypov et al. 2018; Kruger and Latypov 2020). Despite intense studies in this area, studies concerning the exsolution textures in minerals and the sub-solidus evolution of layered intrusions have been rarely reported (Buddington and Lindsley 1964; McConnell 1975). The diverse exsolution textures of Fe-Ti oxides in the rocks of layered intrusions have been suggested to record the variation of temperature and oxygen fugacity (fO_2) of the magma chamber during crystallization and sub-solidus cooling (Haggerty 1991; Frost 1991; Lattard et al. 2007; Brownlee et al. 2010). Understanding the transformation mechanism of these exsolution textures is critical to constrain the sub-solidus cooling processes of layered intrusions.

The ilmenite-hematite ($FeTiO_3$-Fe_2O_3) solid solution (Ilm_{ss}) commonly occurs in layered intrusions (Harrison et al. 2000). Ilm_{ss} tends to experience sub-solidus re-equilibration and phase transformation during different T-fO_2 cooling paths, forming hematite and/or magnetite exsolution and magnetite-rutile intergrowths in ilmenite (Robinson et al. 2002; Tan et al. 2015, 2016; Guo et al. 2017). Experimental results indicate that intergrowths of magnetite-rutile and ilmenite-hematite, which are transformed from Ilm_{ss}, are thermodynamically equivalent over a large temperature interval (Lindsley 1991). However, the magnetite-rutile intergrowth is rare in natural rocks relative to the ilmenite-hematite intergrowth. The interfacial properties of different phases are considered to be critical to the sub-solidus transformation processes (Feinberg et al. 2004; Hammer et al. 2010; Wenk et al. 2011; De Yoreo et al. 2015; Xu et al. 2015, 2017), and may serve to solve this paradox. However, the orientation relationships of Fe-Ti oxides have not yet been investigated so that the effect of interfacial properties of different phases has not been fully understood. The formation of the ilmenite-hematite intergrowth is usually ascribed to the decomposition of Ilm_{ss} when temperature falls below that of the solvus (Harrison et al. 2000). In contrast, the magnetite-rutile intergrowth is likely related to fluids in layered intrusions and metamorphic rocks (Southwick 1968; Tan et al. 2015; Guo et al. 2017). However, there is no direct textural evidence for the oxidation of Ilm_{ss} reported so far. Moreover, it remains enigmatic what controls the oxidizing T-fO_2 trends of the mafic magmas from which the layered intrusions formed.

The fO_2 fluctuation and interfacial properties of the intergrowths have been proposed to be potential factors affecting the sub-solidus transformation of Ilm_{ss} (Lindsley 1991; Rohrer 2010). However, it remains unclear how different intergrowths are developed during the transformation of Ilm_{ss}. In this study, we report both magnetite-rutile symplectite and ilmenite-hematite intergrowth that are transformed from the same Ilm_{ss} precursor in the Xinjie layered intrusion, SW China, and examine the interfacial properties of the two intergrowths and the transformation mechanisms involved. We use electron backscatter diffraction (EBSD) and focused-ion beam–energy dispersive X-ray spectroscopy (FIB-EDS) tomography to investigate the crystallographic orientation, 3-D morphology and texture of the two intergrowths. We also use the compositions of the Fe-Ti oxides to constrain the formation temperature (T) and fO_2 of different intergrowths in the QUILF equilibria (Andersen et al. 1993). This study sheds light on the coherence between diverse exsolution textures of Ilm_{ss} and sub-solidus T-fO_2 trends in a cooling mafic magmatic system. As ilmenite is also ubiquitous in the lunar and martian magmatic rocks (Raymond and Wenk 1971; Wang et al. 2004; Santos et al. 2015), the results in this study can be helpful to the understanding of physicochemical conditions of magmatic processes on the Moon and Mars.

Analytical methods

Electron backscatter diffraction

Thin sections from the analyzed samples were polished with 0.05 μm colloidal silica for 3 hours to allow EBSD analysis. SEM imaging and EBSD analysis were conducted on a Tescan MIRA3 Field Emission SEM, housed in the Microscopy & Microanalysis Facility (John de Laeter Centre) at Curtin University, Perth, Western Australia, and on a FEI Quanta 450 field emission gun SEM housed in the State Key Laboratory and Geological Process and Mineral Resources (GPMR) of China University of Geosciences (Wuhan). The EBSD measurement was performed with an accelerating voltage of 20 kV and a working distance of ~20 mm. Electron Backscatter Patterns (EBSPs) were automatically collected and indexed over a regular grid with a 290 nm step size by using the Oxford Aztec 4.1 software. The CHANNEL 5+ software was used for plotting color-coded maps and the upper hemisphere stereographic pole figures of the indexed mineral. Noise reduction was performed by using a 'wildspike' correction and a five-neighbour zero solution extrapolation.

3D FIB-EDS tomography

The 3D tomography was performed using a Helios G4 Dual Beam Workstation at the Thermo Fisher Scientific Inc., Shanghai. A selected volume was extracted from the area of interest using the focused Ga-ion beam (acceleration voltage 30 kV) for 3D reconstruction. The chemical analyses of Fe, Ti, and O were carried out using acceleration voltage 8 kV, beam current 13 nA. The energy-dispersive X-ray spectroscopy (EDS) analysis was performed in mapping mode to investigate the two dimensional distributions of Fe, Ti, and O. Serial cross-section slices were produced by cutting the selected volume using focused Ga-ion beam, with a distance of 50 nm between slices, and an EDS mapping was collected for every 3 milling steps. The scripting routine is performed automatically with the "Auto slice and view 5.0" software. After data collection, the 2D image sequences were aligned, cropped and stacked into a 3D microstructure image. A total 3D volume of 31.6*11.8*13.25 μm^3 with a voxel pixel of 11.53*11.53*50 nm^3 was reconstructed for further analysis.

Results

Major petrographic features of the Xinjie layered intrusion

The Xinjie intrusion is one of several layered intrusions in the Panzhihua-Xichang region in SW China (Fig. 1a). The intrusion is a NW-SE-striking, sill-like body approximately 7.5 km long, 1-1.5 km wide and 1.2 km thick, and is divided, from the base upwards, into a marginal zone and three lithological cycles (Unit I, II and III) (after Wang et al. 2008). Unit I and II contain different modal proportions of olivine, clinopyroxene, plagioclase and Fe-Ti oxides, forming interlayered wehrlite, olivine gabbro, olivine clinopyroxenite, clinopyroxenite and melagabbro (Fig. 1b). Wehrlite and olivine clinopyroxenite in Units I and II display similar texture, and contain <10 vol.% cumulus and intercumulus magnetite Fe-Ti oxides that are scattered in the rocks (Fig. 2a, b). Hydrous silicates (*e.g.*, amphibole and biotite) are scarce in Units I and II. Unit III is mainly composed of gabbro with < 30 vol.% Fe-Ti oxides (Fig. 2c, d), but it hosts two thick (40-50 m thick) and one thin (~4 m thick) oxide gabbro layers that contain 40-70 vol.% Fe-Ti oxides (Fig. 1b). The rocks of Unit III generally contain 2-5 vol.% hydrous silicates, which are locally gathered and closely associated with Fe-Ti oxides (Fig. 2d).

The exsolution textures in both cumulus and intercumulus ilmenite can be divided into three types, which are distributed unevenly along the profile throughout the intrusion (Fig. 1b). The ilmenite in Unit I and II is generally homogeneous in BSE images and only displays local hematite lamellae (type-I, Fig. 3a, b). The ilmenite in Unit III commonly contains symplectitic intergrowth of magnetite-rutile (type-II, Fig. 3c), and is closely associated with hydrous silicates (Fig. 3d, e). Both type-I and type-II intergrowths are observed in the ilmenite of the melagabbro at the bottom of Unit III, which was then selected to investigate in this study. In addition, the ilmenite in the Fe-Ti oxide gabbro layer of Unit III contains magnetite exsolution (type-III, Fig. 3f).

Appearance of magnetite-rutile symplectite and ilmenite-hematite intergrowth

Magnetite-rutile symplectites in ilmenite comprise micro- to nano-scale anhedral magnetite and rutile (Fig. 4a). The dendritic rutile tends to pinch outwards and is truncated by magnetite (Fig. 4b). The symplectites have discrete and irregular boundaries with the host ilmenite (Fig. 4c). Nano-scale hematite is evenly distributed (Fig. 4d) and oriented parallel to the (0001) planes of the host ilmenite.

Most rutile grains are enveloped by continuous magnetite and show dendritic shape in the 3D images (Fig. 5a and Supplementary movie1). The dendritic rutile looks like isolated in the 2D backscattered electron (BSE) images, but is actually interconnected in the 3D morphology (Fig. 5b and Supplementary movie2). Magnetite appears as connected matrix in the symplectite (Fig. 5c and Supplementary Movie2). Massive lens-like hematite lamellae have sharp contacts with the host ilmenite, forming ilmenite-hematite intergrowth (Fig. 5d).

Compositions of magnetite-rutile symplectite and ilmenite-hematite intergrowth

The EMPA results indicate that rutile in the magnetite-rutile symplectite contains 95.97 to 98.63 wt.% TiO_2 and 1.38 to 3.59 wt.% FeO. Magnetite in the symplectite contains 33.58 to 35.63 wt.% FeO, 59.50 to 63.70 wt.% Fe_2O_3 and 2.72 to 4.68 wt.% TiO_2 (Table 1). The mineral mode of rutile in the symplectite is ~40 wt.% (~45 vol.%), and magnetite is ~60 wt.% (~55 vol.%), so that the symplectite is estimated to contain 21.90 wt.% FeO, 36.82 wt.% Fe_2O_3, and ~41.19 wt.% TiO_2 in bulk composition (Table 1).

The ilmenite-hematite intergrowth contains 41.39-43.05 wt.% FeO, 47.40-49.50 wt.% TiO_2 and 6.76-10.94 wt.% Fe_2O_3 in bulk composition (Table 2). Given that the hematite lamellae mainly contain Fe and O based on the scanning transmission electron mode with energy dispersive spectrometer (STEM-EDS) mapping (Fig. S1), the variation of Fe_2O_3 is likely related to the uneven distribution of nano-scaled hematite lamellae in the intergrowth.

Crystallographic orientation of minerals

The host ilmenite exhibits consistent crystallographic orientation (Fig. 6a, e). The majority of magnetite in the symplectite shares a common $\{1\ 1\ 1\}_{Mag}$ plane, and a set of corresponding $<1\ 1\ 0>_{Mag}$ directions on the common $\{1\ 1\ 1\}_{Mag}$ plane. In detail, there is an angular variation of ~4.5° across the magnetite (Fig. 6b). Similarly, the majority of rutile shares a common $\{1\ 0\ 0\}_{Rut}$ plane and corresponding in-plane $<0\ 0\ 1>_{Rut}$ + $<0\ 1\ 1>_{Rut}$ directions with an angular variation of ~16° (Fig. 6c). The lattice orientations of a single rutile and magnetite grain record the progressive variation of up to ~1.6° and ~3°, respectively (Fig. 6d). Note that the shared $\{1\ 0\ 0\}_{Rut}$ and $\{1\ 1\ 1\}_{Mag}$ planes fall into the same area as the $(0\ 0\ 0\ 1)_{Ilm}$ plane, and the shared $<0\ 0\ 1>_{Rut}$ & $<0\ 1\ 1>_{Rut}$ directions and $<1\ 1\ 0>_{Mag}$ directions also fall into the same area as the $<1\ 0\ -1\ 0>_{Ilm}$ directions (Fig. 6e-g). It is likely that the crystallographic orientations of the majority of magnetite and rutile are controlled by the host ilmenite. Therefore, there is an orientation relationship among the magnetite-rutile symplectites and the host ilmenite, such that $\{1\ 0\ 0\}_{Rut}$ // $\{1\ 1\ 1\}_{Mag}$ // $(0\ 0\ 0\ 1)_{Ilm}$ and ($<0\ 1\ 1>_{Rut}$ + $<0\ 0\ 1>_{Rut}$) // $<1\ 1\ 0>_{Mag}$ // $<1\ 0\ -1\ 0>_{Ilm}$.

The crystallographic projections of both the host ilmenite and hematite lamellae are parallel to each other along the (0 0 0 1) plane (Robinson et al., 2002). The lattice fringes at the ilmenite-hematite interface run straightly across all the directions on the high-resolution transmission electron microscopy (HRTEM) images (Fig. S2).

Discussion

Thermodynamic factors controlling the sub-solidus transformation of Ilm_{ss}

Ilmenite-hematite intergrowths are commonly interpreted as a sub-solidus transformation product of Ilm_{ss} (Robinson et al. 2002). The HRTEM images reveal that the ilmenite and hematite have the same crystallographic orientation and form highly coherent interfaces in the intergrowth (Fig. S2), which can be attributed to their crystallographic similarity (Robinson et al. 2002). The irregular morphologies of magnetite and rutile indicate that the two minerals crystallized concurrently. In addition, the orientation relationships between the magnetite, rutile and host ilmenite indicate that their orientations are inherited from the Ilm_{ss} precursor (Fig. 6e-g). Thus, the ilmenite-hematite intergrowth and the magnetite-rutile symplectite represent two types of transformation products of an Ilm_{ss} precursor.

In general, the Fe-Ti oxides have distinctly different close-packed frameworks for their oxygen atoms; hematite, ilmenite and rutile have "hexagonal close packing" frameworks, whereas magnetite has a "cubic close packing" framework. Hematite and ilmenite have oxygen atoms closely packed or nearly close-packed on the basal (0 0 0 1) plane and along the <1 0 -1 0> direction (Fig. 7a, b). Magnetite has oxygen atoms packed on the $\{1\ 1\ 1\}_{Mag}$ and along the $<1\ 1\ 0>_{Mag}$ (Fig. 7c). Rutile has oxygen atoms packed on the $\{1\ 0\ 0\}_{Rut}$ and along the $<0\ 1\ 1>_{Rut}$ + $<0\ 0\ 1>_{Rut}$ (Fig. 7d). In this study, the inherited orientations of the magnetite-rutile and ilmenite-hematite intergrowths show that their oxygen atom frameworks are aligned consecutively along the interfaces of the two intergrowths.

The sub-solidus transformation of Ilm_{ss} is thermodynamically determined by the total Gibbs free energy change (ΔG) in a Fe-Ti oxide system, which can be expressed as the equation:

$$\Delta G = \Delta G_v + \Delta G_s + \Delta G_\xi$$

where ΔG_v refers to the Gibbs free energy change of phase transformation, ΔG_s refers to the interfacial energy change due to new interface formation, and ΔG_ξ refers to the interfacial strain energy change due to interface lattice misfit. Therefore, ΔG_v is denoted as the driving force of the transformation, whereas ΔG_s and ΔG_ξ are denoted as the energy barriers of the transformation (Rohrer 2010).

As the assemblage of magnetite + rutile are thermodynamically equivalent to that of ilmenite + hematite (Lindsley 1991), the transformation of Ilm_{ss} into the magnetite-rutile symplectite and ilmenite-hematite intergrowth would have the same ΔG_v. Both ΔG_s and ΔG_ξ are determined by the interfacial properties of the Fe-Ti oxides transformed from the Ilm_{ss}, and in turn, the interfacial properties of the Fe-Ti oxides are mainly related to the symmetry and orientation of the oxygen atom framework in each of the Fe-Ti oxides (Feinberg et al. 2004; Wenk et al. 2011). The consecutive oxygen atom frameworks of the two intergrowths as shown in Figure 7 indicate that they share coherent or semi-coherent interfaces (Hammer et al. 2010; De Yoreo et al. 2015). In this case, the ΔG_s can be treated as zero, the energy barrier ΔG_ξ is then the key to determine the transformation path of Ilm_{ss}. The ΔG_ξ can be estimated by the lattice misfit of the oxygen atom framework (δ) at their interfaces (Feinberg et al. 2004; Wenk et al. 2011).

The lattice misfit of the oxygen atom framework along the interface of hematite and ilmenite can be estimated using the oxygen atomic spacing of two minerals, *i.e.*, $\delta_{Ilm\text{-}Hem} = (a_{Ilm} - a_{Hem})/\ a_{Ilm}$, where a_{Ilm} and a_{Hem} refers to the oxygen atomic spacing of ilmenite and hematite, respectively. The $\delta_{Ilm\text{-}Hem}$ is then estimated to be ~1% (Fig. 7a, b). Likewise, the lattice misfit of the oxygen atom framework along the magnetite-rutile interface ($\delta_{Rut\text{-}Mag}$) is estimated to be ~9.8% (Fig. 7c, d). The relatively high $\delta_{Rut\text{-}Mag}$ value would increase the lattice misfit at the interface of magnetite and rutile so that they need to adjust their orientations subtly during coarsening. The intra-grain and inter-grain orientation variations of magnetite and rutile (Fig. 6b-d) could produce high ΔG_{ξ} to hinder the transformation of Ilm_{ss} to the magnetite-rutile intergrowth. In contrast, the low $\delta_{Ilm\text{-}Hem}$ value makes the formation of ilmenite-hematite intergrowth energetically favorable when the temperature falls below the solvus of Ilm_{ss} on sub-solidus cooling, in accordance with its high frequency in natural occurrence.

Transformation of magnetite-rutile symplectite from Ilm_{ss} precursor

The textural relationship shown in 3D images indicates that the dendritic rutile in the magnetite-rutile symplectite is likely the first phase exsolved from the Ilm_{ss}, and predated the matrix magnetite (Figs. 5b, c). The bulk composition of the symplectite is reconstructed to have ~37 wt.% Fe_2O_3 (Table 1), much higher than that for coexisting ilmenite-hematite intergrowth (~8.5 wt.% Fe_2O_3, Table 2), indicating that the formation of the symplectite is related to the oxidation state rather than the isochemical decomposition of the Ilm_{ss} precursor. The exsolution of rutile is ascribed to the sub-solidus oxidation of Fe^{2+} to Fe^{3+} in Ilm_{ss} (Southwick 1968), which can be expressed as $Fe_2O_3 \cdot 5Fe_2TiO_{3\ \text{high Ti-Ilmss}} + O_2 = 3Fe_2O_3 \cdot Fe_2TiO_{3\ \text{low Ti-Ilmss}} + 4TiO_{2\ \text{rutile}}$. The earlier exsolved rutile can act as a crystal seed, and significantly lower the energy barrier needed for coarsening by absorbing Ti^{4+} in the Ilm_{ss}. The exsolved rutile also creates an interface with the Ilm_{ss}. The lattice misfit ($\delta_{Rut\text{-}Ilm} \approx 6.9\%$) at the rutile-$Ilm_{ss}$ interface may cause segregation of Fe^{3+} from the Ilm_{ss} to the interface (Zhang and Zhang 2020), resulting in Fe^{3+} enrichment at the interface. The Ti^{4+} loss and Fe^{3+} enrichment along the rutile-Ilm_{ss} interface facilitate the growth of anhedral magnetite along dendritic rutile (Fig. 5a). Therefore, the transformation of Ilm_{ss} to the magnetite-rutile symplectites stems from the exsolution of rutile in Ilm_{ss}, which is intrinsically attributed to fO_2 elevation during sub-solidus cooling.

T-fO_2 trend for transformation of magnetite-rutile symplectite from Ilm_{ss}

The transformation paths of Ilm_{ss} on the sub-solidus T-fO_2 trends depend on the contents of Fe-Ti oxides, and components of coexisting silicates and fluids (*e.g.*, H_2O and CO_2) in host rocks (Frost 1991). When the rocks are buffered by anhydrous silicates (*e.g.*, clinopyroxene and olivine), Ilm_{ss} follows a slightly oxidizing T-fO_2 trend (QUILF, Fig. 8) and transforms to ilmenite-hematite intergrowths when the temperature falls below the solvus (Harrison et al. 2000). When the rocks contain hydrous silicates (*e.g.*, amphibole and biotite), Ilm_{ss} follows a steeply oxidizing T-fO_2 trend, *e.g.*, the cooling trend of KUIlB (Fig. 8), and transforms to the magnetite-rutile symplectite.

In this study, the bulk composition of the Ilm_{ss} for the investigated sample of the Xinjie intrusion is estimated to be $Ilm_{0.85}Hem_{0.15}$ (Table 2), and coexisting titanomagnetite is $Usp_{0.45}Mag_{0.55}$ (Table S1). Our modeling results indicate that $Ilm_{0.85}Hem_{0.15}$ and $Usp_{0.45}Mag_{0.55}$ can crystallize simultaneously at 952°C and FMQ+0.51 (point "**a**" in Fig. 8). The $Ilm_{0.85}Hem_{0.15}$ may have experienced two-stage transformation along the sub-solidus T-fO_2 trends. Increasing fO_2 of KUIlB would induce "oxy-exsolution" of $Usp_{0.45}Mag_{0.55}$ at ~825°C (point "**b**" in Fig. 8), and the oxidized $Ilm_{0.85}Hem_{0.15}$ at ~550°C would form the magnetite-rutile symplectite (point "**c**" in Fig. 8) and Ti-rich solid solution of $Ilm_{0.92}Hem_{0.08}$. The $Ilm_{0.92}Hem_{0.08}$ is then decomposed into the ilmenite-hematite intergrowth on subsequent cooling (Fig. 8). This can well explain why the two intergrowths could occur in the same ilmenite grains. We infer that the Ilm_{ss} with higher Ti content than $Ilm_{0.85}Hem_{0.15}$ tends to transform to the magnetite-rutile symplectites at temperature above 550 °C when the system is buffered by hydrous silicates (Fig. 8).

Implications

Magma hydration is key to increase the fO_2 of magma (Veksler and Hou, 2020) and modify the crystallization sequence of evolved mafic magmas, triggering crystallization of extensive chromite and Fe-Ti oxide in layered intrusions (Reynolds 1985; Pang et al. 2008; Boudreau 2016; Veksler and Hou, 2020). This study reveals that the magnetite-rutile symplectite in Ilm_{ss} is essentially developed associated with the mineral assemblages crystallized from hydrated magmas. Therefore, the magnetite-rutile symplectite transformed from Ilm_{ss} can provide important clues of magma hydration, which is critical to understanding the subsolidus cooling history and related chromite/ Fe-Ti oxide mineralization of layered intrusions elsewhere.

Water is also of importance to the evolution and crystallization of lunar and martian magmas (Gross et al. 2013; Hui et al. 2013; Filiberto et al. 2019). Although primary hydrous minerals in the lunar and martian rocks are direct evidence for hydrated magmas, they may be obscured by hydrothermal alteration, metamorphism, weathering, solar wind implantation and meteorite impacts (Spandler et al., 2005; Sharp et al. 2013; Hui et al. 2013; Jolliff et al. 2019). On the other hand, ilmenite is ubiquitous in the martian and lunar rocks (Haggerty 1991; Wang et al. 2004; Santos et al. 2015) and is less susceptible to subsequent overprints. Primary textures that formed during crystallization and sub-solidus cooling can be well preserved in ilmenite (*e.g.*, Fig. 3). Therefore, magnetite-rutile symplectites may be an indicator of magma hydration in martian and lunar magmas even when other hydrous phases are no longer present.

Acknowledgement This study was financially supported by National Key R&D Program of China (2018YFA0702600), NFSC grant (41921003), Department of Science and Technology of Guangdong Province (2017GC010578), and Science and Technology Planning of Guangdong Province, China (2017B030314175/ 2020B1212060055). We thank Shun Guo for the constructive suggestions, and Devin Wu, Wendy Chen and Haifeng Gao for the assistance in sample preparation and 3D FIB-EDS tomography. We would also like to thank B. R. Frost, Josh M. Feinberg, Haijun Xu, Sarah Brownlee and an anonymous colleague for critical and constructive comments.

References

Andersen, D. J., Lindsley, D. H., and Davidson, P. M. (1993) QUILF: A pascal program to assess equilibria among Fe-Mg-Mn-Ti oxides, pyroxenes, olivine, and quartz. Computers & Geosciences, 19, 1333-1350.

Boudreau, A.E. (2016) The Stillwater Complex, Montana–Overview and the significance of volatiles. Mineralogical Magazine, 80, 585-637.

Brownlee, S.J., Feinberg, J.M., Harrison, R.J., Kasama, T., Scott, G.R., and Renne, P.R., (2010) Thermal modification of hematite-ilmenite intergrowths in the Ecstall pluton, British Columbia, Canada. American Mineralogist, 95, 153-160.

Buddington, A.F., and Lindsley D.H. (1964) Iron-Titanium Oxide Minerals and

Synthetic Equivalents. Journal of petrology, 5, 310-357.

De Yoreo, J.J., Gilbert, P.U.P.A., Sommerdijk, N.A.J.M., Penn, R.L., Whitelam, S., Joester, D., Zhang, H.Z., Rimer, J.D., Navrotsky, A., Banfield, J.F., Wallace, A.F., Michel, F.M., Meldrum, F.C., Cölfen, H., and Dove, P.M. (2015) Crystallization by particle attachment in synthetic, biogenic, and geologic environments. Science, 349, aaa6760-1- aaa6760-9.

Feinberg, J.M., Wenk, H.R., Renne, P.R., and Scott, G.R. (2004) Epitaxial relationships of clinopyroxene-hosted magnetite determined using electron backscatter diffraction (EBSD) technique. American Mineralogist, 89, 462-466.

Filiberto, J., McCubbin, F.M., and Taylor, G.J. (2019) Volatiles in martian magmas and the interior: Inputs of volatiles into the crust and atmosphere. Volatiles in the Martian Crust, 13-33, Elsevier.

Frost, B.R. (1991) Magnetic petrology: factors that control the occurrence of magnetite in crustal rocks. Reviews in Mineralogy and Geochemistry, 25, 489-509.

Gross, J., Filiberto, J., and Bell, A.S. (2013) Water in the martian interior: Evidence for terrestrial MORB mantle-like volatile contents from hydroxyl-rich apatite in olivine–phyric shergottite NWA 6234. Earth and Planetary Science Letters, 369, 120-128.

Guo, S., Tang, P., Su, B., Chen, Y., Ye, K., Zhang, L.M., Gao, Y.J., Liu, J.B., and Yang, Y.H. (2017) Unusual replacement of Fe-Ti oxides by rutile during retrogression in amphibolite-hosted veins (Dabie UHP terrane): A mineralogical record of fluid-induced oxidation processes in exhumed UHP slabs. American Mineralogist, 102, 2268-2283.

Haggerty, S.E. (1991) Oxide textures; a mini-atlas. Reviews in Mineralogy and

Geochemistry, 25, 129-219.

Hammer, J.E., Sharp, T.G., and Wessel, P. (2010) Heterogeneous nucleation and epitaxial crystal growth of magmatic minerals. Geology, 38, 367-370.

Harrison, R.J., Becker, U., and Redfern, S.A.T. (2000) Thermodynamics of the R$\bar{3}$ to R$\bar{3}$c phase transition in the ilmenite-hematite solid solution. American Mineralogist, 85, 1694-1705.

Holness, M.B., Nielsen, T.F., Tegner, C. (2017) The Skaergaard intrusion of East Greenland: paradigms, problems and new perspectives. Elements, 13, 391-396.

Hui, H., Peslier, A.H., Zhang, Y., and Neal, C.R. (2013) Water in lunar anorthosites and evidence for a wet early Moon. Nature Geoscience, 6, 177-180.

Jolliff, B.L., Mittlefehldt, D.W., Farrand, W.H., Knoll, A.H., McLennan, S.M., and Gellert, R. (2019) Mars Exploration Rover Opportunity. Water and Other Volatiles on Ancient Mars: Volatiles in the Martian Crust, 285-328, Elsevier.

Kruger, W., and Latypov, R. (2020) Fossilized solidifications fronts in the Bushveld Complex argues for liquid-dominated magmatic systems. Nature Communications, 11, 1-11.

Latypov, R., Costin, G., Chistyakova, S., Hunt, E.J., Mukherjee, R., and Naldrett, T. (2018) Platinum-bearing chromite layers are caused by pressure reduction during magma ascent. Nature Communications, 9, 1-7.

Lindsley, D.H. (1991) Experimental studies of oxide minerals. Reviews in Mineralogy and Geochemistry, 25, 69-106.

McBirney, A.R., Hunter, R.H. (1995) The cumulate paradigm reconsidered. The journal of Geology, 103, 114-122.

McConnell, J. (1975) Microstructures of minerals as petrogenetic indicators. Annual Review of Earth and Planetary Sciences, 3, 129-155.

Pang, K.N., Zhou, M.F., Lindsley, D.H., Zhao, D., Malpas, J. (2008) Origin of Fe-Ti oxide ores in mafic intrusions: Evidence from the Panzhihua intrusion, SW China. Journal of Petrology, 49, 295-313.

Raymond, K., and Wenk, H. (1971) Lunar ilmenite (refinement of the crystal structure). Contributions to mineralogy and petrology, 30, 135-140.

Reynolds, I.M. (1985) The nature and origin of titaniferous magnetite-rich layers in the upper zone of the Bushveld Complex; a review and synthesis. Economic Geology, 80, 1089-1108.

Robinson, P., Harrison, R.J., McEnroe, S.A., and Hargraves, R.B. (2002) Lamellar magnetism in the haematite–ilmenite series as an explanation for strong remanent magnetization. Nature, 418, 517-520.

Rohrer, G.S. (2010) "Introduction to Grains, Phases, and Interfaces-an Interpretation of Microstructure," Trans. AIME, 1948, vol. 175, pp. 15-51, by CS Smith. Metallurgical and Materals Transactions A, 41A, 1063-1063.

Santos, A.R., Agee, C.B., McCubbin, F.M., Shearer, C.K., Burger, P.V., Tartese, R., and Anand, M. (2015) Petrology of igneous clasts in Northwest Africa 7034: Implications for the petrologic diversity of the Martian crust. Geochimica et Cosmochimica Acta, 157, 56-85.

Spandler, C., Mavrogenes, J., Arculus, R. (2005) Origin of chromitites in layered intrusions: Evidence from chromite-hosted melt inclusions from the Stillwater Complex. Geology, 33, 893-896.

Sharp, Z.D., McCubbin, F.M., and Shearer, C.K. (2013) A hydrogen-based oxidation mechanism relevant to planetary formation. Earth and Planetary Science Letters, 380, 88-97.

Southwick, D.L. (1968) Mineralogy of a rutile and apatite-bearing ultramafic chlorite rock, Harford county, Maryland. US Geological Survey Prof. Paper, 600, C38-C44.

Tan, W., Wang, C.Y., He, H.P., Xing, C.M., Liang, X., and Dong, H. (2015) Magnetite-rutile symplectite derived from ilmenite-hematite solid solution in the Xinjie Fe-Ti oxide-bearing, mafic-ultramafic layered intrusion (SW China): American Mineralogist, 100, 2348-2351.

Tan, W., He, H.P., Wang, C.Y., Dong, H., Liang, X.L., and Zhu, J.X. (2016) Magnetite exsolution in ilmenite from the Fe-Ti oxide gabbro in the Xinjie intrusion (SW China) and sources of unusually strong remnant magnetization. American Mineralogist, 101, 2759-2767.

Veksler, I. V., and Hou, T. (2020) Experimental study on the effects of H_2O upon crystallization in the Lower and Critical Zones of the Bushveld Complex with an emphasis on chromitite formation. Contributions to Mineralogy and Petrology, 175, 85(1-17).

Wang, A., Kuebler, K.E., Jolliff, B.L., and Haskin, L.A. (2004) Raman spectroscopy of Fe-Ti-Cr-oxides, case study: Martian meteorite EETA79001. American Mineralogist, 89, 665-680.

Wang, C.Y., Zhou, M.F., and Zhao, D.G. (2008) Fe-Ti-Cr oxides from the Permian Xinjie mafic-ultramafic layered intrusion in the Emeishan large igneous province, SW China: Crystallization from Fe- and Ti-rich basaltic magmas. Lithos, 102, 198-217.

Wenk, H.R., Chen, K., and Smith, R. (2011) Morphology and microstructure of magnetite and ilmenite inclusions in plagioclase from Adirondack anorthositic gneiss. American Mineralogist, 96, 1316-1324.

Xu, H., Zhang J., Zong, K., and Liu L. (2015) Quartz exsolution topotaxy in clinopyroxene from the UHP eclogite of Weihai, China. Lithos, 226, 17-30.

Xu, H., and Wu, Y. (2017) Oriented inclusions of pyroxene, amphibole and rutile in garnet from the Lüliangshan garnet peridotite massif, North Qaidam UHPM belt, NW China: An electron backscatter diffraction study. Journal of Metamorphic Geology, 35, 1-17.

Zhang, X., and Zhang, Y. (2020) Effects of local geometry distortion at the Al/Al_2Cu interfaces on solute segregation. Physical Chemistry Chemical Physics, 22, 4106-4114.

Figure captions:

Fig. 1. Geological background and lithological characters of the Xinjie intrusion. **(a)** A schematic geological map of the Xinjie intrusion in the Emeishan Large Igneous Province (ELIP) in SW China; **(b)** A stratigraphic column that cuts through the Xinjie intrusion showing the major rock types, distribution of Fe-Ti oxides, and exsolution types in ilmenite in the intrusion. Note there are three types of exsolution textures in ilmenite, including Type-I (ilmenite-hematite intergrowth), Type-II (magnetite-rutile symplectite) and Type-III (magnetite exsolution).

Fig. 2. The occurrences of silicates and Fe-Ti oxides from different lithological units of the Xinjie intrusion. **(a)** Anhedral and euhedral Fe-Ti oxides as interstitial phases among clinopyroxene in **Unit I**, transmitted light; **(b)** Elongated and anhedral Fe-Ti oxides as interstitial phases among silicates in **Unit II**, transmitted light; **(c)** Cumulus Fe-Ti oxides in the Fe-Ti oxide gabbro at the bottom of **Unit III**, transmitted light; **(d)** Anhedral and euhedral Fe-Ti oxides, amphibole and biotite as interstitial phases among plagioclase in **Unit III**. Ol, olivine; Cpx, clinopyroxene; Pl, plagioclase; Amp, amphibole; Bt, biotite.

Fig. 3. BSE images of ilmenite grains hosting different types of exsolution textures in the Xinjie intrusion. **(a)** Euhedral ilmenite as inclusions in silicates showing no exsolution (**Type-I**) in **Unit I**; **(b)** Elongated ilmenite showing well-oriented hematite lamellae (**Type-I**) in **Unit II**; **(c)** Occurrence of magnetite-rutile symplectite (**Type-II**) in ilmenite grain from the leucogabbro in **Unit III**; **(d)** Biotite coexisting with plagioclase and ilmenite hosting magnetite-rutile symplectite (**Type-II**) from the olivine gabbro at the bottom of **Unit III**; **(e)** Amphibole coexisting with plagioclase, titanomagnetite and ilmenite hosting magnetite-rutile symplectite (**Type-II**) from the olivine gabbro at the bottom of **Unit III,** note the skeletal titanomagetite (left) formed by sub-solidus reaction; **(f)** Occurrences of magnetite (**Type-III**) in different ilmenite grains coexisted with cumulus titanomagnetite in the Fe-Ti oxide gabbro at the bottom of **Unit III**. Ilm, ilmenite; Hem, hematite; Tmt, titanomagnetite; Sym, symplectite; Mag, magnetite.

Fig. 4. Textures in ilmenite from the melagabbro of Unit III in the Xinjie intrusion, sample X-327. (a) magnetite-rutile symplectite in ilmenite (Ilm); **(b)** vermicular rutile (Rut) occurs as a core and magnetite (Mag) presents as connected matrix in the magnetite-rutile symplectite; **(c)** Miniscule magnetite and rutile present near the boundary of the magnetite-rutile symplectite; **(d)** well-oriented nano-scale hematite (Hem) lamellae parallel to the (0001) plane of the host ilmenite.

Fig. 5. Three-dimensional morphologies of magnetite-rutile symplectite in ilmenite. (a) typical occurrence of rutile, magnetite and hematite in ilmenite; **(b)** dendritic rutile and isolated rutile grains, note that the dendritic rutile is interconnected; **(c)** magnetite surrounding large dendritic rutile grain; **(d)** nano-scale, lens-like hematite lamellae homogeneously distributed in ilmenite.

Fig. 6. Microstructure and orientation for the major phases in the magnetite-rutile symplectite and host ilmenite constructed from EBSD data. (a) Phase-color map of magnetite (Mag, green), rutile (Rt, fuchsia) and host ilmenite (Ilm); **(b)** magnetite lattice orientation variations to 4.5° from the red cross (TC_Mag, texture component for magnetite); **(c)** rutile lattice orientation variations to 16° from the red cross (TC_Rt, , texture component for rutile); **(d)** Grain reference orientation deviation angle (GROD angle) showing the deviation angle from the average orientation of a rutile grain and its surrounding magnetite; **(e-g)** lower hemisphere equal area projection patterns of host ilmenite, magnetite matrix and vermicular rutile, colored with their phase colors in **(a)**. The circles and triangles indicate the parallel planes and directions of different minerals, respectively. Note: the data on each model indicate the periodic distance of every four oxygen atoms along <1 0 -1 0>Ilm, <1 0 -1 0>Hem, <1 1 0>Mag, and <0 1 1>Rut + <0 0 1>Rut, respectively.

Fig. 7. Space filling models showing the symmetries of oxygen atom frameworks of (a) ilmenite, (b) hematite, (c) magnetite and (d) rutile on their specific orientations.

Fig. 8. The diagram of Δlog fO_2 (FMQ) versus Temperature showing the isopleths of Fe-Ti oxide solid solution and the cooling trend of KUIlB buffer (biotite-ilmenite-feldspar-ulvöspinel) (modified after Frost, 1991 and Harrison et

al., 2000). Oxygen fugacity and temperature determined by QUILF-95 at P = 5 kbar (Table S2); Usp10 refers to solid solution of $Ulvöspinel_{10}$-$Magnetite_{90}$ (in molar fraction) and Ilm70 refers to $Ilmenite_{70}$-$Hematite_{30}$, and so on; $\Delta\log fO_2$ refers to the FMQ buffer; "**a**" refers to the crystallization T-fO_2 condition for $Ilm_{0.85}Hem_{0.15}$ coexisting $Usp_{0.45}Mag_{0.55}$, "**b**" refers to the T-fO_2 condition for "oxy-exsolution" of $Usp_{0.45}Mag_{0.55}$, and "**c**" refers to the T-fO_2 condition for transformation of $Ilm_{0.85}Hem_{0.15}$ to magnetite-rutile symplectite and ilmenite-hematite intergrowth.

TABLE 1. Major oxide compositions of rutile and magnetite in the magnetite-rutile symplectite (in wt.%)

Major oxides	Rutile						Magnetite							Bulk composition* (in average)
	1	2	3	4	5	6	1	2	3	4	5	6	7	
SiO_2	0.02	0.01	0.02	0.00	0.01	0.02	0.02	0.01	0.00	0.00	0.27	0.01	0.00	**0.03 (0)**
MgO	0.01	0.02	0.01	0.04	0.03	0.03	0.05	0.02	0.00	0.00	0.00	0.00	0.01	**0.02 (0)**
Al_2O_3	0.00	0.01	0.00	0.02	0.02	0.02	0.00	0.01	0.01	0.00	0.04	0.01	0.00	**0.01 (0)**
FeO*	2.43	2.91	1.38	2.63	3.59	2.87	34.91	33.58	34.01	35.06	34.85	35.63	35.12	**22.14 (0.69)**
Fe_2O_3*	-	-	-	-	-	-	59.50	63.70	62.15	61.68	61.41	60.42	60.68	**37.28 (1.33)**
MnO	0.02	0.01	0.00	0.00	0.00	0.00	0.04	0.01	0.00	0.00	0.00	0.01	0.02	**0.01 (0)**
NiO	0.00	0.00	0.00	0.00	0.00	0.00	0.08	0.09	0.09	0.01	0.07	0.05	0.05	**0.04 (0)**
Cr_2O_3	0.00	0.00	0.00	0.03	0.03	0.00	0.02	0.03	0.02	0.03	0.02	0.01	0.00	**0.01 (0)**
TiO_2	97.77	96.63	98.63	97.29	95.97	96.43	4.50	2.72	3.36	4.06	3.64	4.68	4.34	**40.48 (2.02)**
Total	100.24	99.59	100.03	100.01	99.64	99.36	99.11	100.16	99.64	100.84	100.30	100.81	100.21	**100.02 (0.01)**

*Notes: Redistribution of the measured ΣFeO between Fe_2O_3 and FeO is on the basis of charge balance and stoichiometry of magnetite; the average bulk composition of the rutile-magnetite symplectite is based on the modal proportion analysis of rutile/ magnetite ratios on BSE images, rutile takes up ~45 vol.% (~40 wt.%) and magnetite ~55 vol.% (~60 wt.%) in average; standard deviations have listed in the parentheses.

TABLE 2. Bulk major oxide compositions of ilmenite-hematite intergrowth (in wt.%)

Major oxides	1	2	3	4	5	6	7	8	9	10	Average	Bulk composition including two intergrowths
SiO_2	0.00	0.00	0.00	0.02	0.01	0.01	0.01	0.03	0.02	0.00	**0.01 (0.01)**	**0.02 (0)**
MgO	0.33	0.34	0.35	0.35	0.35	0.33	0.35	0.34	0.33	0.32	**0.34 (0.01)**	**0.16 (0.03)**
Al_2O_3	0.00	0.00	0.00	0.01	0.00	0.00	0.01	0.00	0.00	0.00	**0 (0)**	**0.01 (0)**
FeO*	42.06	43.03	42.77	42.90	42.31	43.24	42.32	41.39	41.75	43.05	**42.54 (0.63)**	**39.55 (0.64)**
Fe_2O_3*	9.42	7.54	8.14	7.86	8.93	6.76	8.56	10.94	10.66	7.59	**8.45 (1.32)**	**14.78 (1.35)**
MnO	0.67	0.65	0.74	0.66	0.71	0.67	0.65	0.66	0.61	0.65	**0.67 (0.02)**	**0.35 (0.07)**
NiO	0.03	0.01	0.00	0.02	0.00	0.05	0.00	0.01	0.03	0.00	**0.02 (0.02)**	**0.02 (0.01)**
Cr_2O_3	0.03	0.00	0.00	0.04	0.03	0.00	0.01	0.01	0.00	0.00	**0.01 (0.01)**	**0.02 (0.01)**
TiO_2	48.17	49.25	49.08	49.12	48.52	49.50	48.45	47.40	47.75	49.22	**48.70 (0.70)**	**44.72 (0.87)**
Total	100.70	100.83	101.08	100.97	100.86	100.55	100.35	100.78	101.14	100.83	**100.73 (0.01)**	**99.65 (0.26)**
											X_{Ilm} = 0.92 **X_{Hem} = 0.08**	**$X_{Ilm} \approx$ 0.85** **$X_{Hem} \approx$ 0.15**

*Notes: Redistribution of the measured ΣFeO between Fe_2O_3 and FeO is on the basis of charge balance and stoichiometry of ilmenite; the bulk composition including the ilmenite-hematite intergrowth and the rutile-magnetite symplectite; the modal proportions of symplectite in different ilmenite grains range from 34% to 58%, and the resulted standard deviations of the bulk composition are listed in the parentheses; X_{Ilm} and X_{Hem} refer to mole fractions of ilmenite and hematite, respectively; standard deviations have listed in the parentheses.

Fig.1

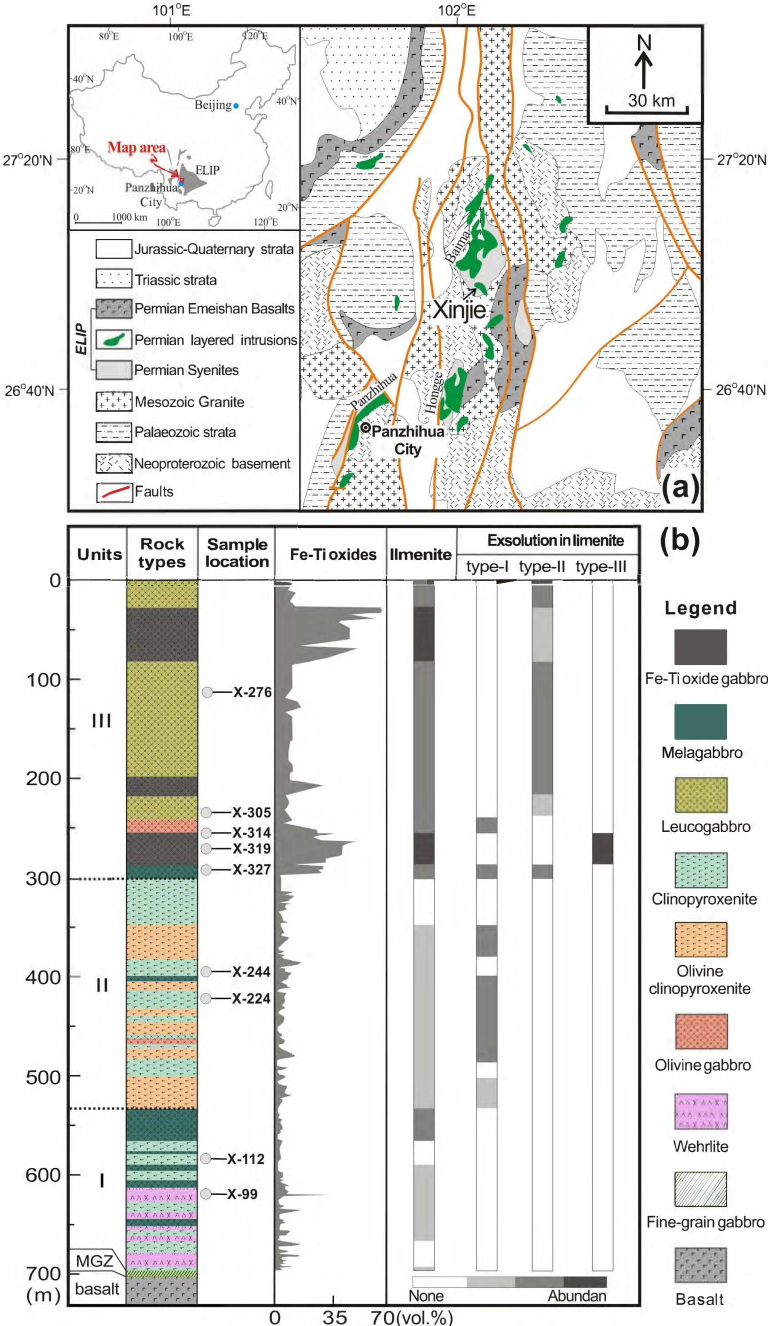

101°E
102°E
80°E
100°E
120°E
40°N
Beijing
Map area
ELIP
Panzhihua City
20°N
1000 km
N
30 km
27°20'N
26°40'N
Jurassic-Quaternary strata
Triassic strata
Permian Emeishan Basalts
Permian layered intrusions
Permian Syenites
Mesozoic Granite
Palaeozoic strata
Neoproterozoic basement
Faults
ELIP
Baima
Xinjie
Panzhihua
Hongge
Panzhihua City
(a)
(b)
Units
Rock types
Sample location
Fe-Ti oxides
Ilmenite
Exsolution in ilmenite
type-I
type-II
type-III
III
II
I
MGZ
basalt
X-276
X-305
X-314
X-319
X-327
X-244
X-224
X-112
X-99
0
100
200
300
400
500
600
700
(m)
0
35
70(vol.%)
None
Abundan
Legend
Fe-Ti oxide gabbro
Melagabbro
Leucogabbro
Clinopyroxenite
Olivine clinopyroxenite
Olivine gabbro
Wehrlite
Fine-grain gabbro
Basalt

Fig.2

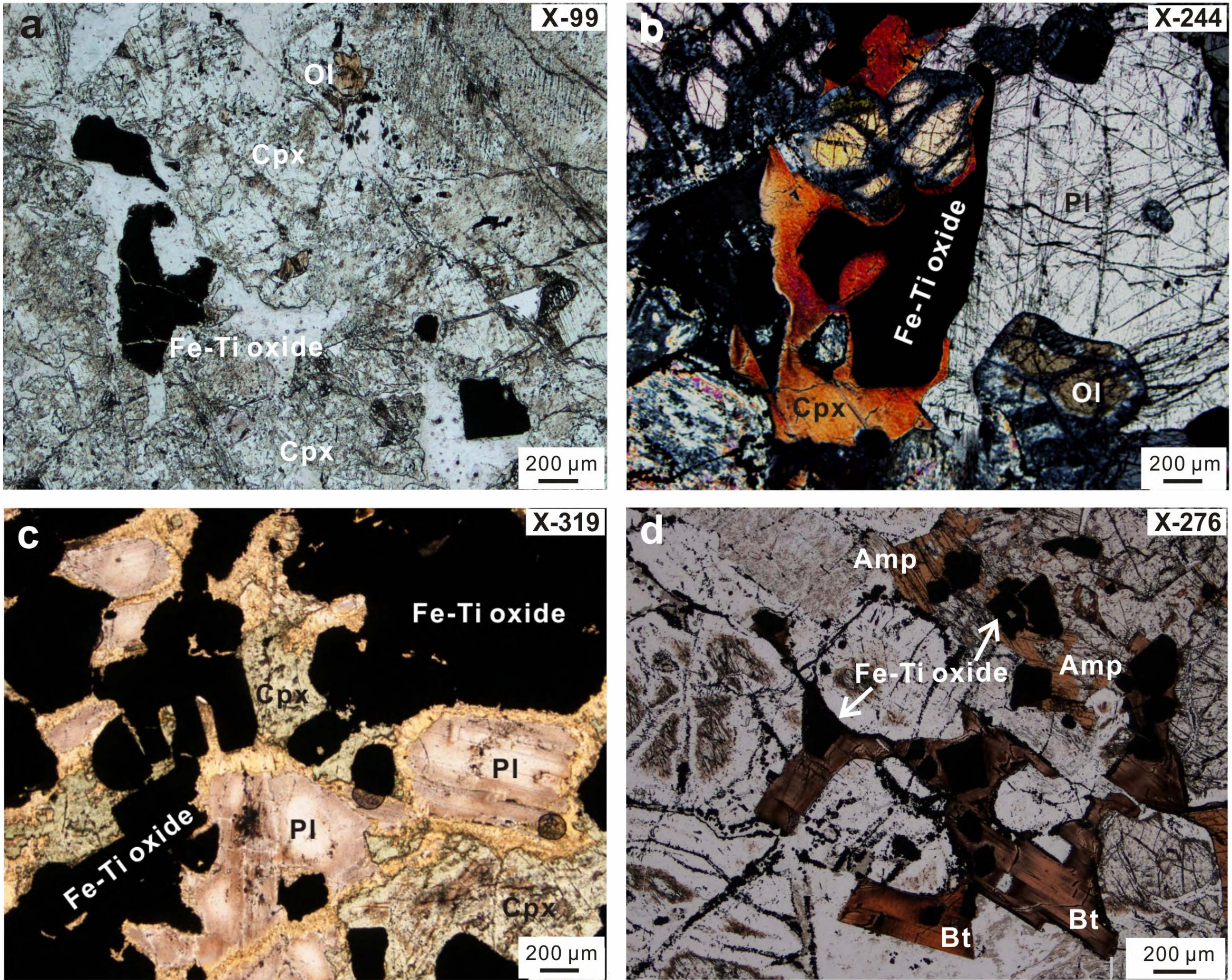

a
X-99
Ol
Cpx
Fe-Ti oxide
Cpx
200 μm
b
X-244
Pl
Fe-Ti oxide
Ol
Cpx
200 μm
c
X-319
Fe-Ti oxide
Cpx
Pl
Pl
Fe-Ti oxide
Cpx
200 μm
d
X-276
Amp
Fe-Ti oxide
Amp
Bt
Bt
200 μm

Fig.3

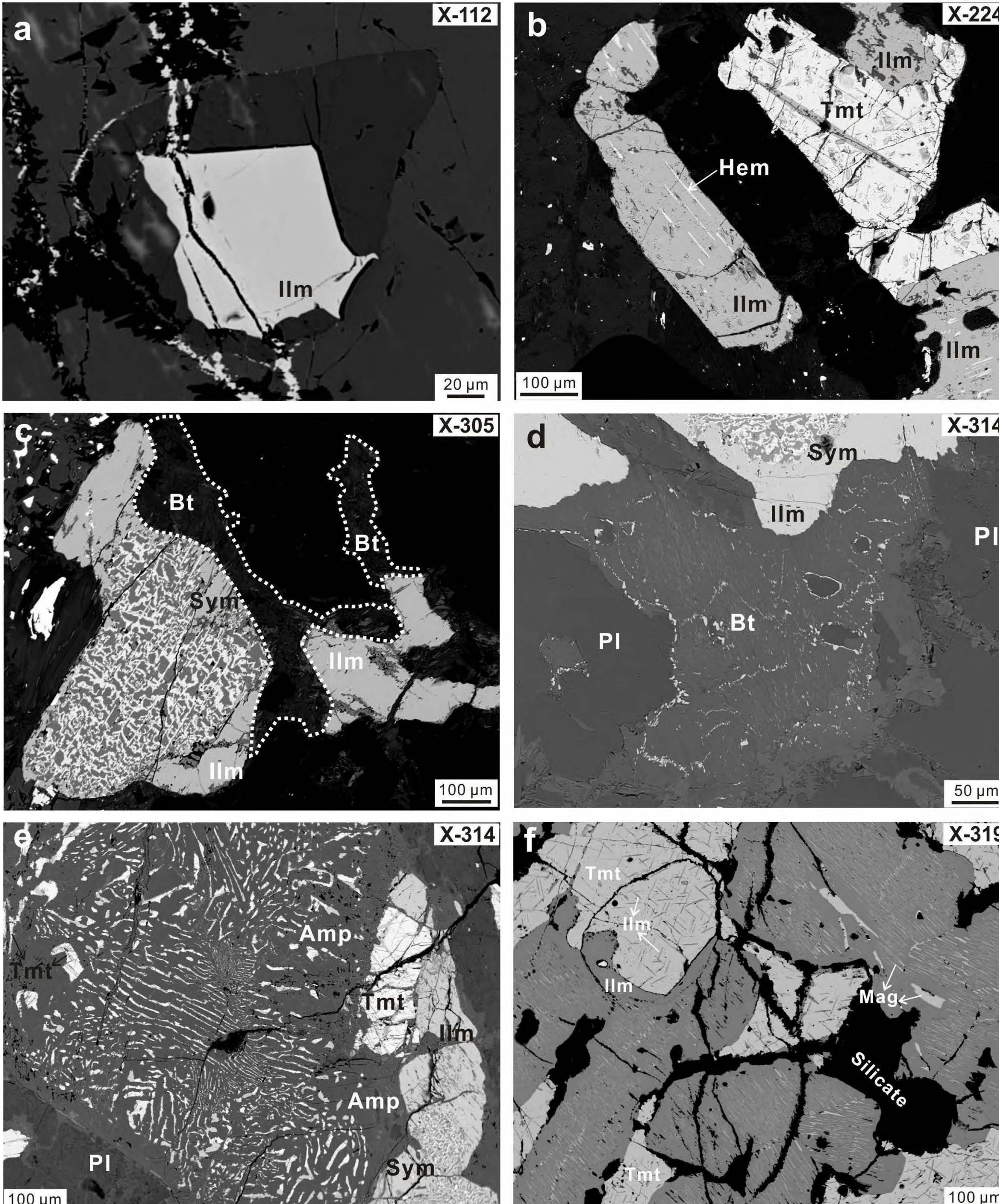
a
X-112
Ilm
20 μm
b
X-224
Ilm
Tmt
Hem
Ilm
Ilm
100 μm
c
X-305
Bt
Bt
Sym
Ilm
Ilm
100 μm
d
X-314
Sym
Ilm
Pl
Bt
Pl
50 μm
e
X-314
Amp
Tmt
Tmt
Ilm
Amp
Pl
Sym
100 μm
f
X-319
Tmt
Ilm
Ilm
Mag
Silicate
Tmt
100 μm

Fig.4

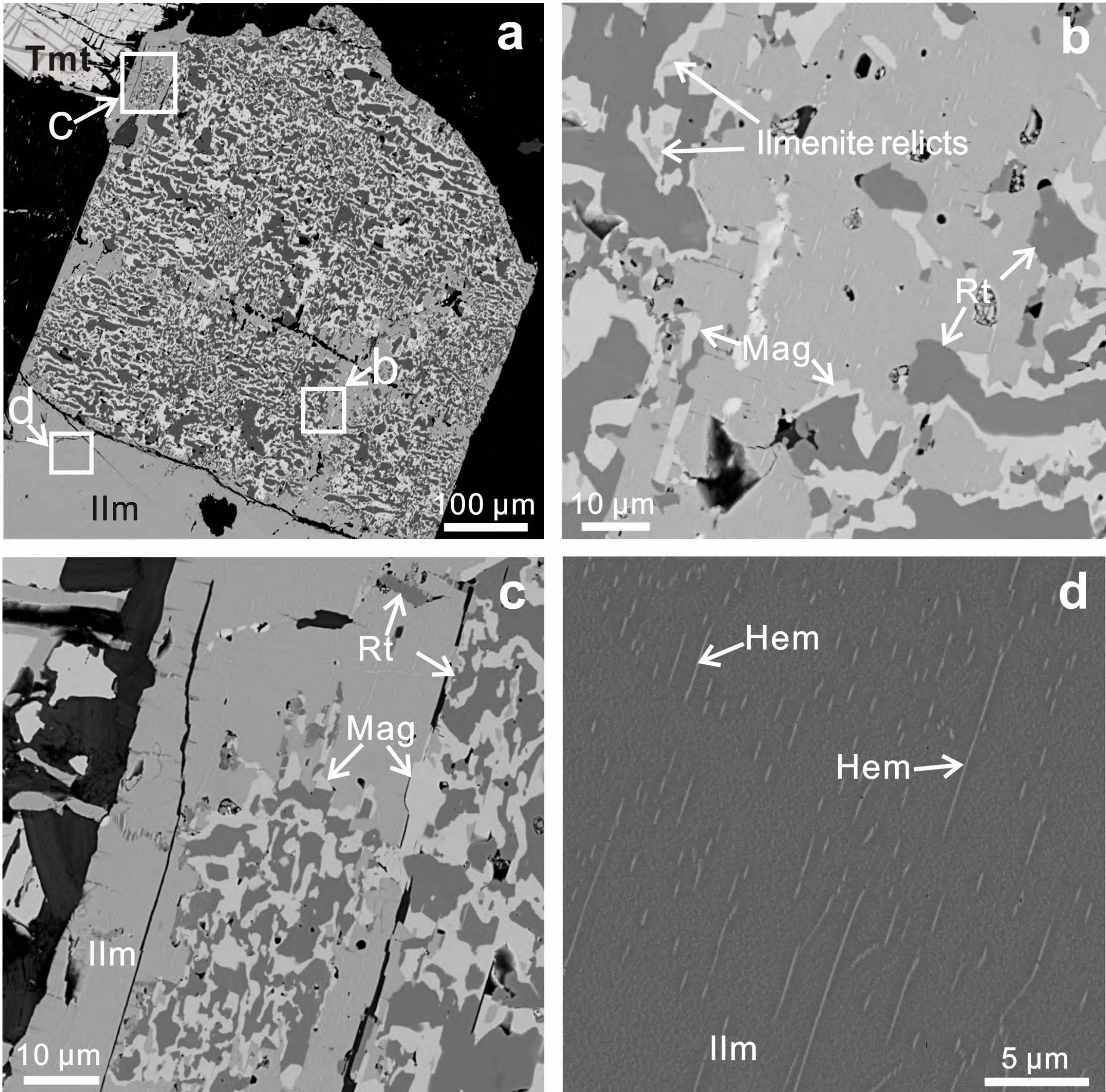
a
Tmt
c
b
d
Ilm
100 μm
b
Ilmenite relicts
Rt
Mag
10 μm
c
Rt
Mag
Ilm
10 μm
d
Hem
Hem
Ilm
5 μm

Fig.5

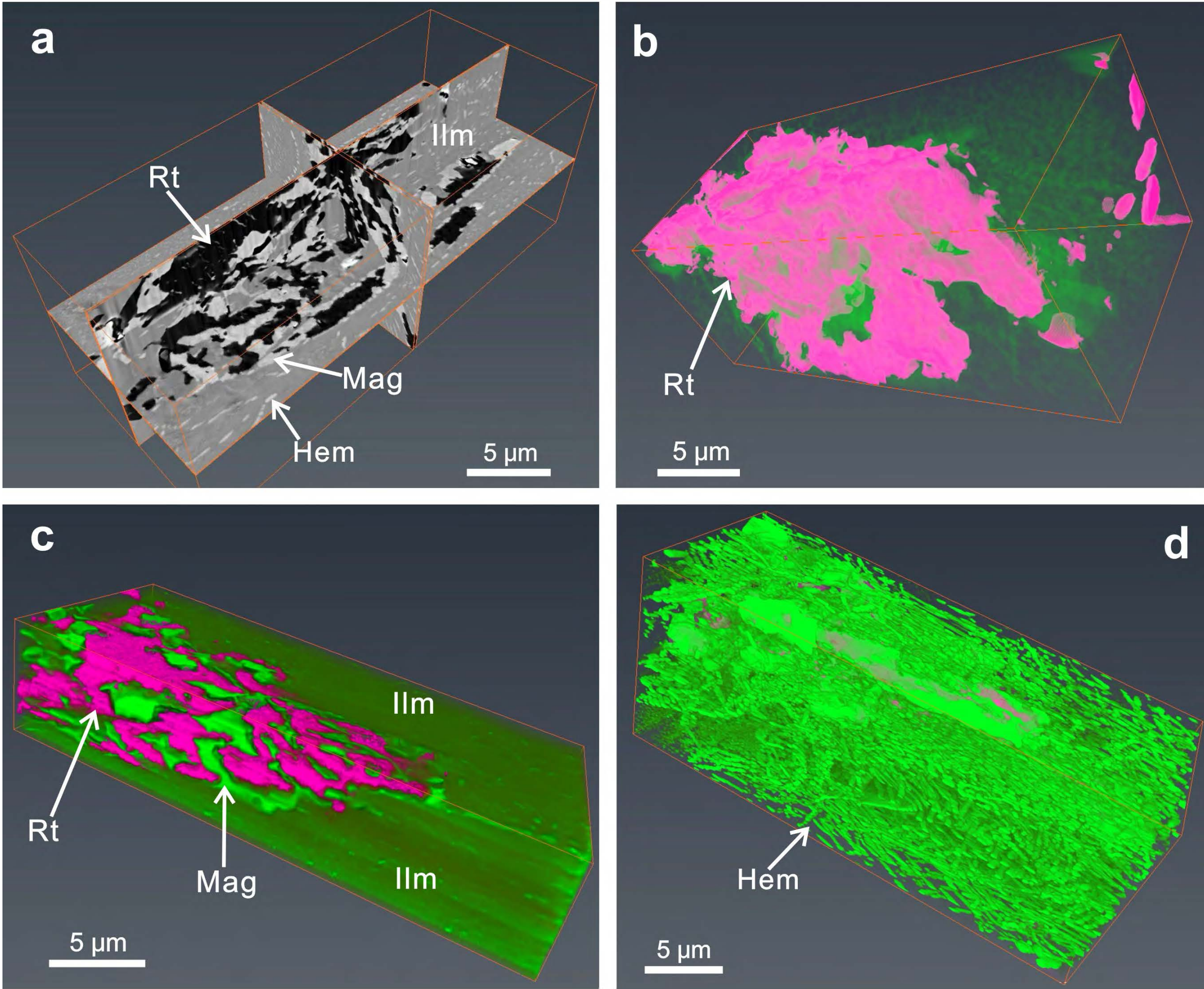

Fig.6

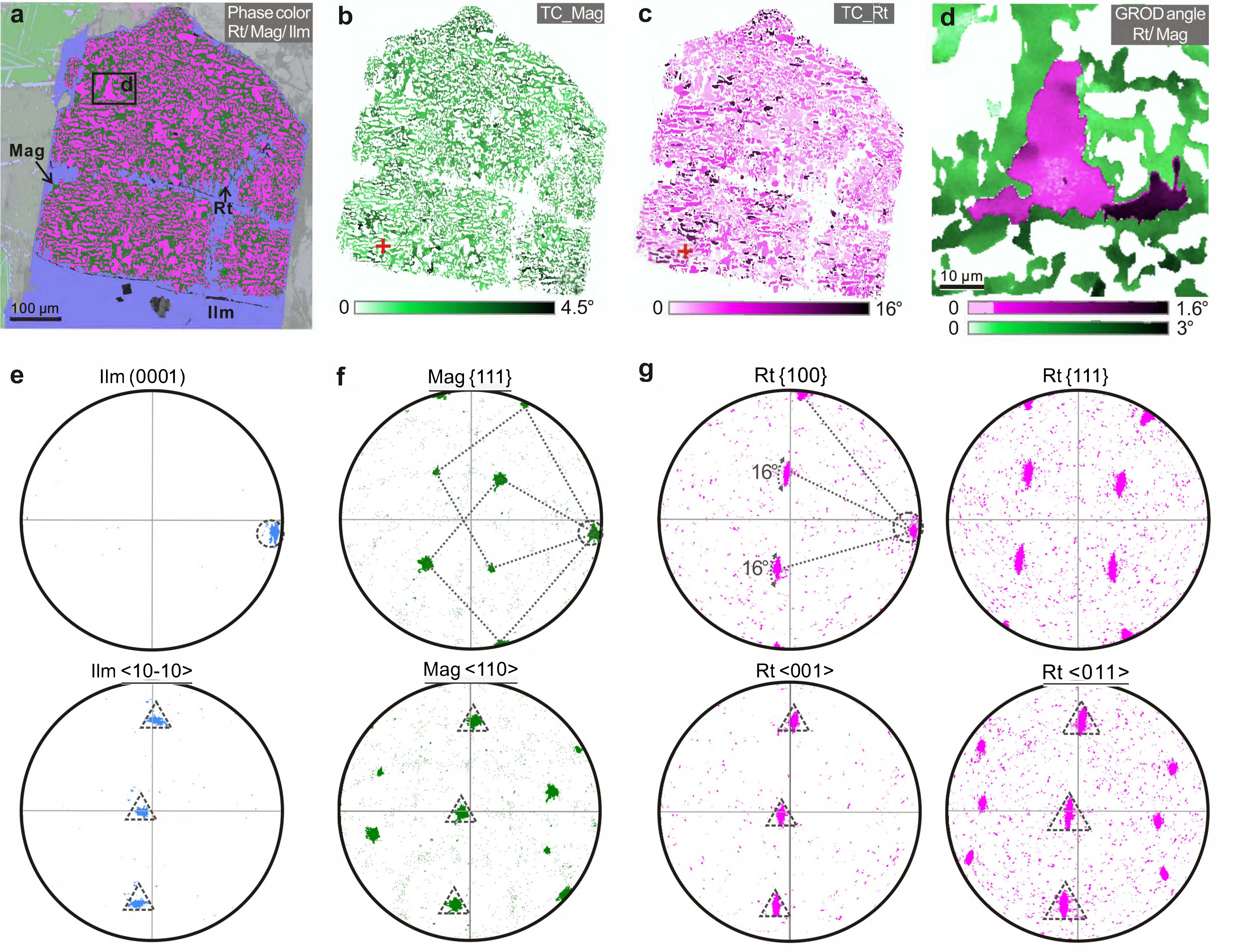

a
Phase color
Rt/ Mag/ Ilm
d
Mag
Rt
100 μm
Ilm
b
TC_Mag
0
4.5°
c
TC_Rt
0
16°
d
GROD angle
Rt/ Mag
10 μm
0
1.6°
0
3°
e
Ilm (0001)
Ilm <10-10>
f
Mag {111}
Mag <110>
g
Rt {100}
16°
16°
Rt {111}
Rt <001>
Rt <011>

Fig.7

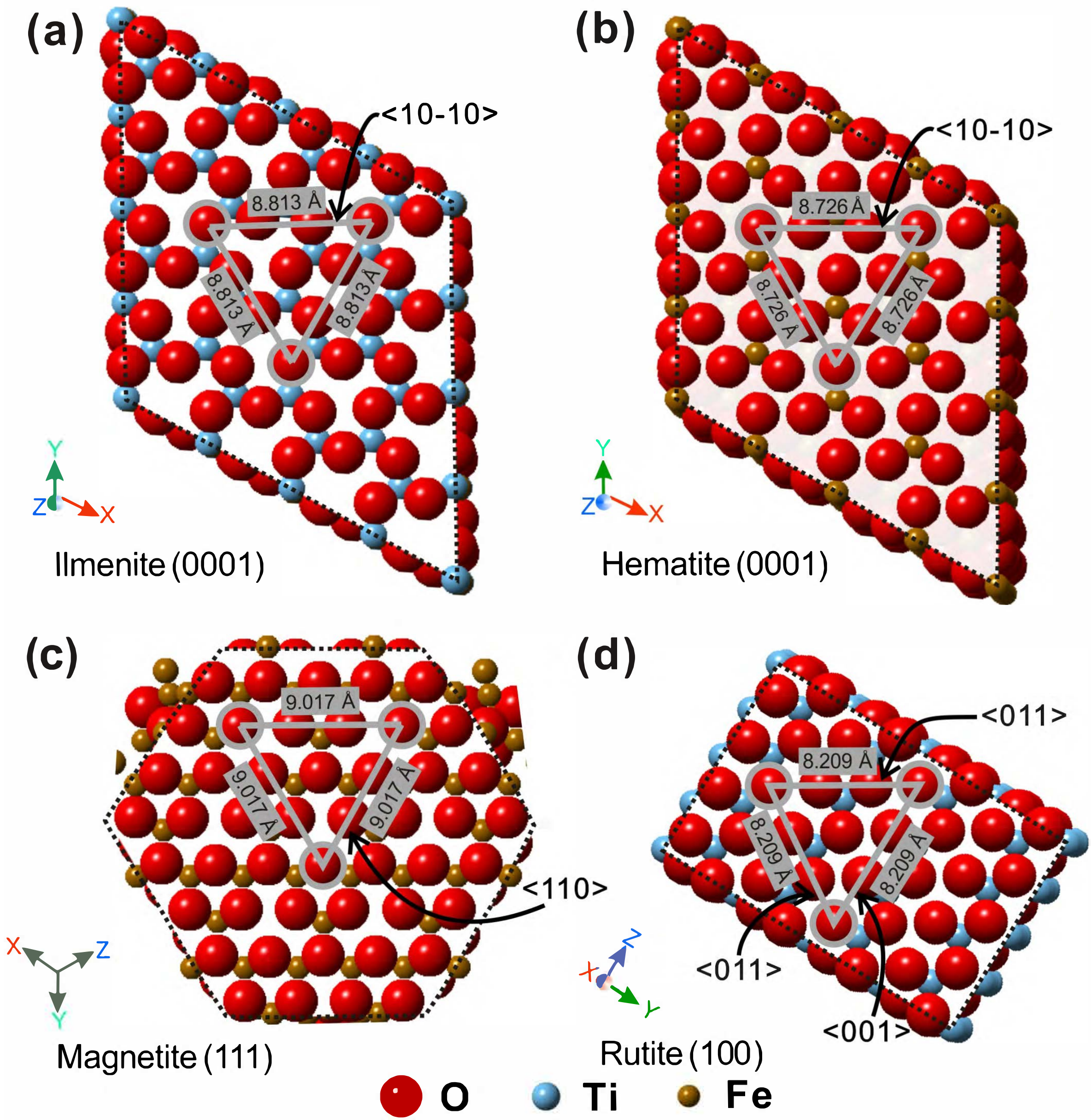
(a)
<10-10>
8.813 Å
8.813 Å
8.813 Å
Y
Z
X
Ilmenite (0001)
(b)
<10-10>
8.726 Å
8.726 Å
8.726 Å
Y
Z
X
Hematite (0001)
(c)
9.017 Å
9.017 Å
9.017 Å
<110>
X
Z
Y
Magnetite (111)
(d)
<011>
8.209 Å
8.209 Å
8.209 Å
<011>
<001>
Z
X
Y
Rutite (100)
O
Ti
Fe

Fig.8

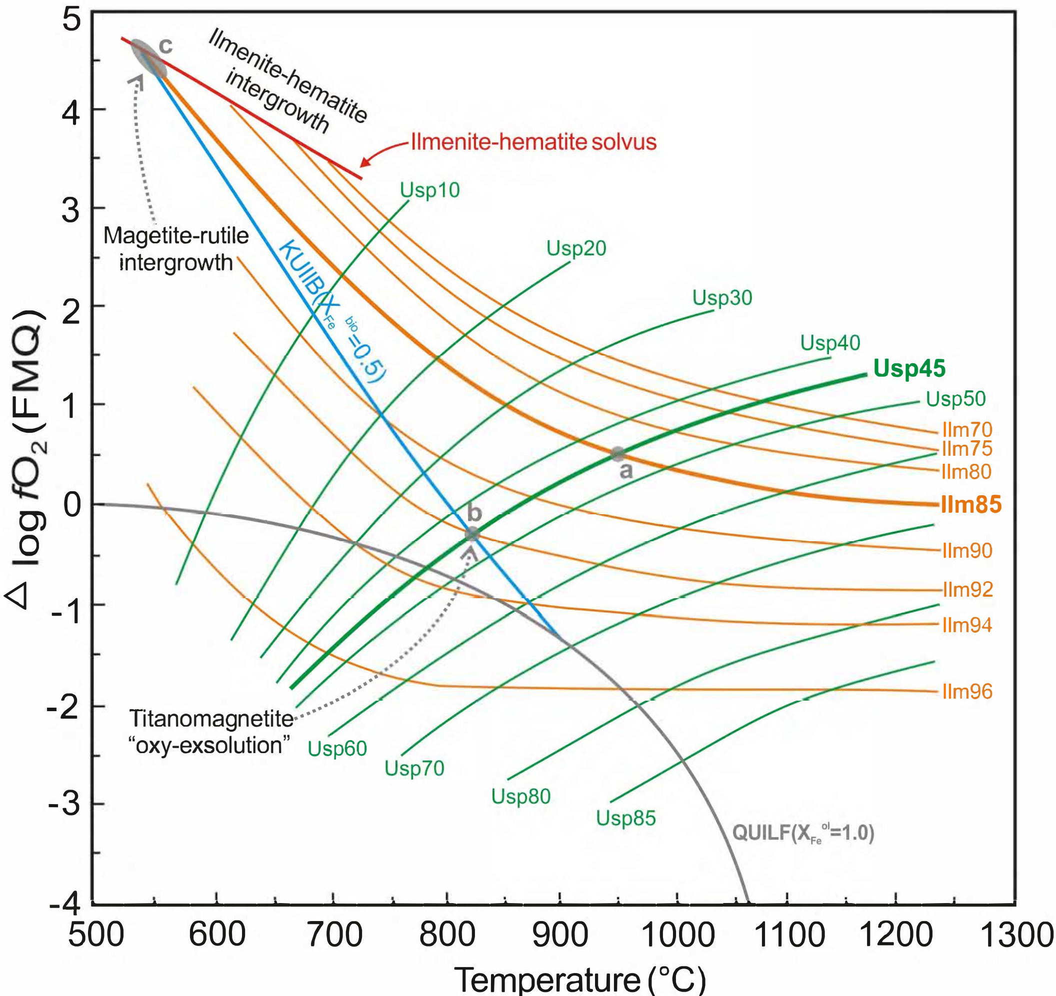

Ilmenite-hematite intergrowth
Ilmenite-hematite solvus
c
Magetite-rutile intergrowth
KUIIB(X_{Fe}^{bio}=0.5)
Usp10
Usp20
Usp30
Usp40
Usp45
Usp50
Ilm70
Ilm75
Ilm80
Ilm85
Ilm90
Ilm92
Ilm94
Ilm96
a
b
Titanomagnetite "oxy-exsolution"
Usp60
Usp70
Usp80
Usp85
QUILF(X_{Fe}^{ol}=1.0)
Δ log fO$_2$ (FMQ)
Temperature (°C)
5
4
3
2
1
0
-1
-2
-3
-4
500
600
700
800
900
1000
1100
1200
1300